Pure Appl. Geophys. 172 (2015), 1269–1290

DOI 10.1007/s00024-014-0958-9

Pure and Applied Geophysics

Microstructures Induced in Porous Limestone by Dynamic Loading, and Fracture Healing: An Experimental Approach

Julie Richard,[1,2] Mai-Linh Doan,[1,2] Jean-Pierre Gratier,[1,2] and François Renard[1,2,3]

Abstract—Fracturing and healing are crucial processes inducing changes in the permeability and mechanical behavior of fault zones. Fracturing increases the permeability of fault rocks, creating flow-channels for fluid circulation and enhancing the kinetics of such fluid–rock processes as pressure solution or metamorphism. Conversely, healing processes reduce permeability by closing the fractures and lead to rock strengthening. Consequently, the timescales of these two processes are important in determining the strength of fault zones and their ability to rupture during earthquakes. This article reports observations of the microstructure of porous limestone samples subjected to rapid dynamic loading, and long-term healing as a result of fluid percolation. Dynamic loading was performed by impacting the samples with steel bars inside a split Hopkinson pressure bar apparatus. Healing was performed by leaving the samples for three months within a triaxial machine with percolation of supersaturated fluids for five weeks. Two kinds of fracture network were observed in samples damaged at high strain rate: a series of radial and circular macrofractures and an incipient pulverization zone at the center of the sample loaded at the highest strain rate. Fracture density determined microscopically from X-ray images correlates with dissipated energy computed from macromechanical data. X-ray images enable good quantification of the damaged state of the samples. Percolation experiments under stress with high-solubility fluid at room temperature show that the main healing processes promoting closure of the fractures in the sample are a combination of mechanical and chemical compaction. Microfracturing networks were found to heal faster than the largest fractures, leading to heterogeneous strengthening of the rock. This feature affects the processes of earthquake nucleation and rupture propagation.

1. Introduction

The networks of fractures in fault damage zones result from cumulative damage as a result of repeated earthquakes and creep deformation during interseismic periods (Tenthorey and Cox 2006). The internal structure of fault damage zones is important to the mechanical properties of the whole fault zone (Faulkner *et al.* 2003) and to strain distribution across the fault core, which can be either localized or homogeneous (Rutter *et al.* 1986; De Paola *et al.* 2008; Faulkner *et al.* 2010). Moreover, Faulkner *et al.* (2006) showed that stress rotations in a weak fault occur inside the damage zone surrounding the fault core. Fracture and healing are two major mechanisms that strongly affect the mechanical behavior of active faults. They are involved in different fault processes, leading to strengthening or weakening of fault zones. Given that their dependence on different conditions varies from one fault to another, and because of the scarcity of in-situ observations, defining the extent of these two mechanisms remains challenging.

In nature, dynamic loading of rock is associated with seismic deformation, either from large earthquakes or from microseismicity, and may cause rock pulverization. An extreme example of off-fault damage is the pulverized rock located next to sections of some major strike–slip faults, for example the San Andreas Fault (Dor *et al.* 2006a; Wechsler *et al.* 2011). They reflect the need to understand the damage processes in these areas, because they can provide important information on rupture propagation during an earthquake (Dor *et al.* 2006a, b), on earthquake propagation velocity, and on the dynamic effects responsible for gouge formation (Reches and Dewers 2005). They also help distinguish between damage related to fault processes and surface-weathering (Wechsler *et al.* 2011).

Several experimental studies have been performed to enable understanding of the propagation of cracks

[1] ISTerre, Univ. Grenoble Alpes, BP 53, 38041 Grenoble, France. E-mail: francois.renard@ujf-grenoble.fr
[2] ISTerre, CNRS, BP 53, 38041 Grenoble, France.
[3] Department of Geosciences, PGP, University of Oslo, 0316 Oslo, Norway.

(Ravi-Chandar and Knauss 1984a, b; Sagy *et al.* 2001; Renard *et al.* 2009a) and the transition between damaged to pulverized rocks (Doan and Gary 2009; Dor *et al.* 2009; Yuan *et al.* 2011; Doan and Billi 2011). Such experiments emphasize the dependence of fracture mechanisms on different conditions, the most important being strain rate, total strain, and material characteristics (Doan and Gary 2009; Doan and Billi 2011). They also provide evidence that fracturing activates such fluid–rock reaction processes as pressure solution creep, which are involved in healing mechanisms and, consequently, in the processes controlling changes in fault strength (Weyl 1959; Rutter 1976; Raj 1982; Sleep and Blanpied 1992; Gratier *et al.* 1999, 2003; van Noort *et al.* 2008; Gratier 2011).

Several mechanisms on different time scales induce fault healing. One healing process responsible for rapid recovery of the strength of faults is inelastic yielding on contact asperities, as revealed by the experiments of Dieterich and Kilgore (1996). Other healing processes, for example compaction by pressure solution creep or fracture sealing, occur on longer time scales, making it difficult to observe the entire mechanism in nature. The competition between damage and healing can have major effects on earthquake and fault processes. Specific examples of this are given in Ben-Zion (2008) and are based on theoretical results in a viscoelastic brittle damage model (Ben-Zion *et al.* 1999; Lyakhovsky *et al.* 2001). Quantifying these processes is therefore crucial for better understanding the dynamics of the seismic cycle.

Some seismological results for in-situ healing of fault damage zones have been obtained and show either logarithmic or power-law time dependence of healing and creep. For example, using seismic data Wu *et al.* (2009) documented significant co-seismic damage (e.g., 30–50 %) during the Düzce earthquake, followed by log (*t*) healing involving substantial recovery on a sub-day time scale and slower progressive recovery over months (Peng and Ben-Zion 2006). Gratier *et al.* (2014) compared experiments with post-seismic data for the Izmit earthquake and proposed that pressure solution creep enhanced by damage could produce a power law post-seismic creep which could fit geodetic deformation data.

Healing experiments enhanced by pressure solution processes can be performed under specific conditions (high solid solubility, high temperature, etc.), thus avoiding the time scale issue (Brantley *et al.* 1990; Hickman and Evans 1991; Cox and Paterson 1991; Karner *et al.* 1997; Bos and Spiers 2002; Hellmann *et al.* 2002a, b; Nakatani and Scholz 2004; Yasuhara *et al.* 2005; Tenthorey and Cox 2006; Le Guen *et al.* 2007; Niemeijer *et al.* 2008). These studies show that healing processes depend on pressure and temperature conditions, and on the fluid chemistry and mineralogical characteristics of the material. In general, fracturing and healing experiments are performed on single crystals or on monomineralic aggregates (with the exception of granitic rocks: Morrow *et al.* 2001; Moore *et al.* 1994; Tenthorey and Fitzgerald 2006). But rocks have a complex structure and are heterogeneous on different scales, especially for materials with high porosity, for example some natural carbonates or fault gouge rocks. Microscale heterogeneities affect the geometry of fracture propagation (Renard *et al.* 2009a) and the rate of healing.

In this study we conducted damage and healing experiments on the same natural rock to simulate the damage and healing sequence of the seismic cycle. We first simulated coseismic damage by loading samples with split Hopkinson pressure bars, to create the dense fracture damage expected at high strain rate (Doan and Gary 2009). To understand healing and sealing processes, long-term percolation experiments were conducted, under triaxial (differential stress) conditions, on pre-damaged and pristine samples. The purpose was to investigate the effect of both non-stress-driven self-healing (Brantley *et al.* 1990; Renard *et al.* 2000) and stress-driven sealing and/or compaction mechanisms (Bos and Spiers 2002; Gratier *et al.* 2003). These experiments should, therefore, be long enough to enable some fluid–rock chemical interaction. To stay within reasonable time spans (several months) we used limestone, because carbonate rocks are more reactive, with porosity high enough to enable fast fluid percolation.

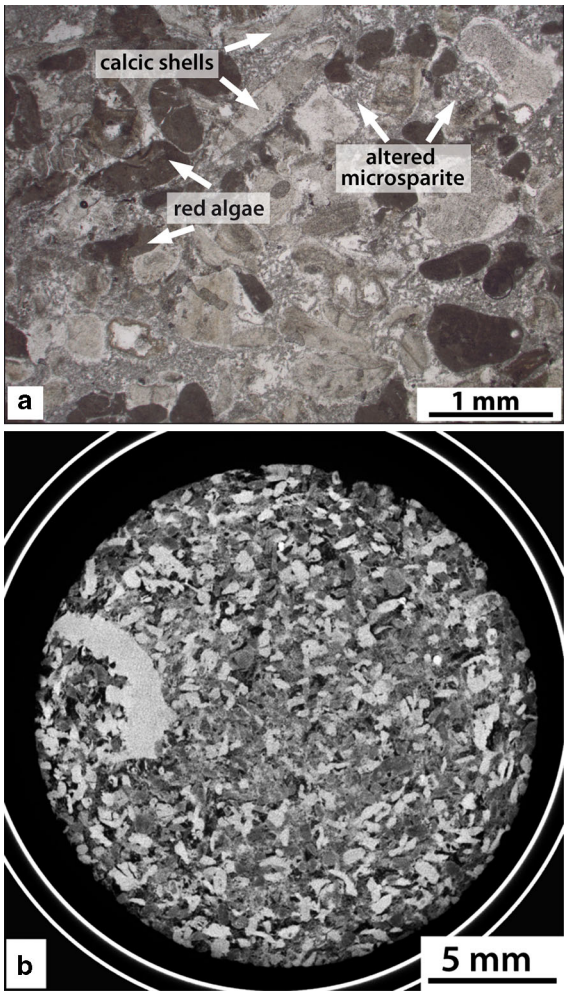

Figure 1
a Optical microscopy image of a representative thin section of a sample of Estaillades limestone in its initial state. The *dark grains* correspond to red algae debris and the *light grey grains* correspond to calcitic shells. The grains are embedded in a microsparitic cement. **b** X-ray tomography images of one slice of a sample of Estaillades limestone before deformation. *Black holes* are porosity, the *dark grey grains* correspond to the red algae debris, the *white grains* to calcitic shells, and the microsparitic cement is in *light grey*. The size distribution of the calcitic shell and red algae grains covers a range of 100–5,000 μm

Table 1
Characteristics of the two samples used in healing experiments

	C1 (Undamaged)	C3 (Damaged)
Diameter (mm)	24.9	24.8
Weight (g)	44.53	24.27
l_0 height (mm)	49.3	25
l (mm)	46.05	25.65
ε (strain)	−0.066	0.026
$\dot{\varepsilon}$ (strain rate, s^{-1})	-10^{-8}	$7.1.10^{-9}$
σ_A (axial stress, MPa)	14.6	1.5
P_f (fluid pressure, MPa)	1	1
σ_L (lateral stress, MPa)	2.1	2
T (°C)	20	20
Fluid flow (m^3 s^{-1})	5.10^{-9}	5.10^{-9}
Tomography acquisition	Initial − After percolation	After loading (initial) − After percolation
FEG-SEM images	Initial state (preserved after percolation on undamaged sample) Fig. 11a–f	Deformed state after fracturing (loading) and percolation (dissolution and healing) Fig. 12a–f

2. Experimental Materials and Procedures

2.1. Sample Material

The limestone samples were collected in Estaillades quarry (South East France). This Cretaceous bioclastic limestone has a porosity close to 30 % and a permeability of 270 mD (Le Guen *et al.* 2007). It was chosen because of its relatively high permeability, typical of a reservoir rock, and its millimetric heterogeneities that act as stress concentrators during deformation. It is a weak material with a uniaxial confining stress value of 12 MPa. This limestone contains fossil grains of algae of millimeter size, and broken calcitic shells, with dimensions in the range 0.6 to more than 1 mm, embedded in microsparitic cement (Fig. 1a). Two types of porosity were observed: inter-granular macro-pores which are well connected (size approx. 500 μm), and intra-granular micro-pores found in some red algae fossil grains (Han *et al.* 2007; Dautriat *et al.* 2011) of size approximately 10–50 μm.

Samples of different size were used (Tables 1, 2). The diameter and height of the samples was varied to minimize boundary effects related to the two deformation instruments used in this study. Images of each sample were taken by X-ray tomography (Laboratoire

Table 2

Characteristics of the samples deformed under dynamic loading tests and fracture density measured on tomography data

	CHB1	CHB2	CHB3	CHB4	C3
Weight (g)	10.6	10.6	10.8	11	24.27
Height (mm)	20	19.7	20	19.8	25
Diameter (mm)	19.1	19.5	19.5	19.1	24.8
Impact velocity (m s^{-1})	4	3	3.5	4.5	6.7
Peak stress (MPa)	13	12	11	19	56
Maximum strain (%)	0.9	0.6	1	1.2	2.3
Maximum strain rate (s^{-1})	78	78	73	84	570
Dissipated energy (MJ/m^3)	0.072	0.028	0.059	0.12	0.77

	Slice #	Total area (mm^2)	Fracture area (mm^2)	Fracture density (%)	Density average (%)
Initial state	–	–	–	–	0.3 ± 0.3
CHB2	216	293.7	1.3	0.4	0.7 ± 0.4
	526	293.7	1.9	0.6	
	876	293.7	1.2	0.4	
	1331	293.7	3.8	1.3	
CHB3	152	293.7	5.2	1.8	2.0 ± 0.8
	507	293.7	7.4	2.5	
	847	293.7	6.4	2.2	
	1232	293.7	4.9	1.6	
CHB1	179	286.5	7.6	2.6	2.9 ± 1
	514	286.5	6.7	2.3	
	884	286.5	8.9	3.1	
	1184	286.5	9.6	3.4	
CHB4	309	286.5	8.3	2.9	3.7 ± 1.2
	509	286.5	8.5	3	
	934	286.5	13.2	4.6	
	1193	286.5	13	4.5	
C3 initial	214	535.3	85.4	16	18.8 ± 10.4
	430	535.3	81.4	15.2	
	864	535.3	111.3	20.8	
	1049	535.3	123.3	23	
C3 final	1026	451.3	35.6	7.9	7.1 ± 3.6
	816	451.3	28.8	6.4	

3SR, UMR 5521 CNRS, Univ. Grenoble-Alpes), to characterize its initial microstructure before deformation (Fig. 1b). After each experiment, another image of each sample was obtained, for comparison with the initial state. Finally, some thin sections were produced after the experiments and were observed by scanning electron microscopy.

2.2. Dynamic Loading and Percolation Experiments

2.2.1 The Hopkinson Bar Apparatus for Dynamic Loading of Samples

The experiments were performed by use of a split Hopkinson pressure bar (SHPB) apparatus, which enables samples to be damaged at high strain rate (Doan and Gary 2009; Chen and Song 2010), at ISTerre, Grenoble, France (Fig. 2a). Another sample of larger diameter (C3; Table 1) was deformed in the Laboratoire de Mécanique des Solides of the Ecole Polytechnique, Palaiseau, France. Each sample was fixed between two steel bars 2 cm in diameter and 1.5 m long. It is then loaded by a striker impacting the bar assembly and launched by a spring gun. The striker velocity determines the strain rate and the maximum stress level reached. The striker length determines the loading duration (here ~70 µs, for the ISTerre bars). Both bars are equipped with two strain gauges located near the input edge and the center of each bar. These strain gauges measure the incident, reflected, and transmitted elastic waves which can be used to determine

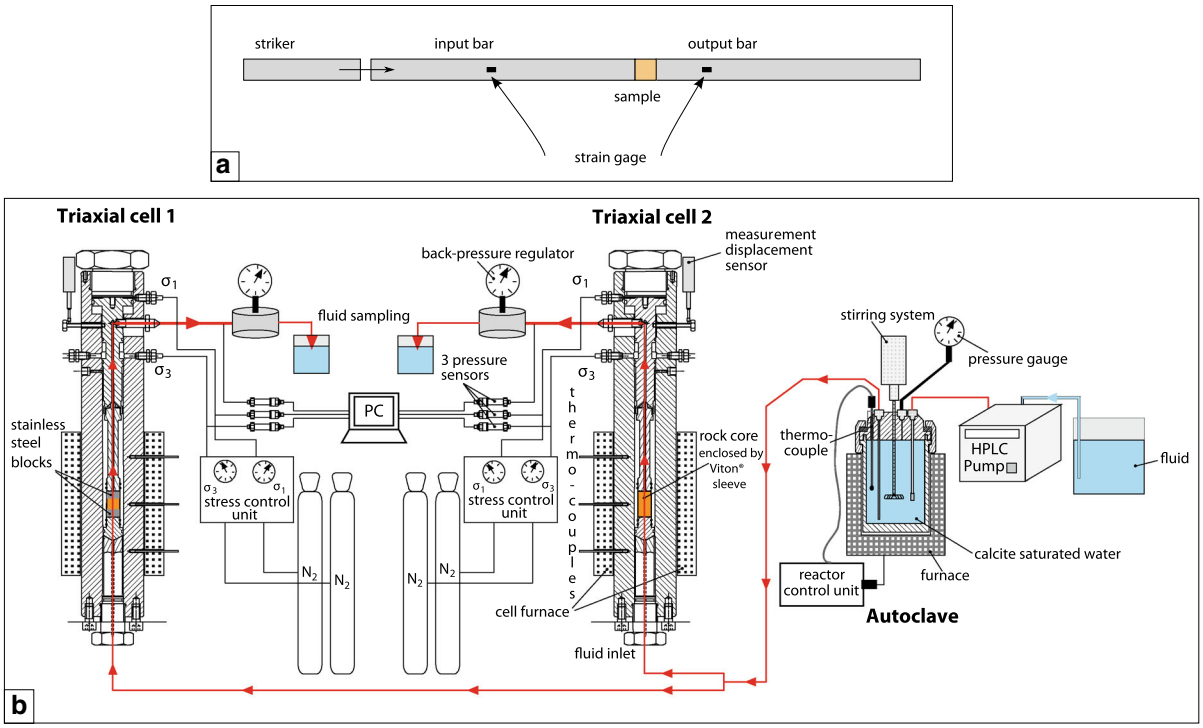

Figure 2
a Sketch of the split Hopkinson pressure bars (SHPB). **b** Sketch of the triaxial cells coupled to percolation. Most often the uniaxial stress is the maximum stress σ_1, the confining pressure or the lateral stress is the minimum stress (σ_3), but the lateral stress may be chosen to be slightly higher than the axial stress, and P_f is the fluid pressure. These three conditions and the injection rate were all separately controlled and measured. The calcite-saturated water was prepared in a separate pressure vessel (modified after Le Guen *et al.* 2007)

the stress and strain history of the sample (Chen and Song 2010).

Two sets of experiments were conducted separately. We first prepared a highly comminuted, but still cohesive, sample for the healing experiments. This sample was 2.5 cm in diameter and jacketed with a thick Viton sleeve. It was loaded at Ecole Polytechnique on a large SHPB device, able to damage the sample substantially. The strength of the sample was 56 MPa, with a high loading rate of 567 s^{-1}. The second kind of experiment was performed at ISTerre, on a smaller set of bars, designed to load smaller samples, only 2 cm in diameter, at smaller strain. For the latter experiments the strain rate achieved was almost independent of the striker speed, within the range 70–80 s^{-1}. In total, five experiments were performed under different loading conditions, controlled by the speed of the striker (Table 2). The fracture density for each sample after induction of damage with the SHPB apparatus was measured by use of X-ray tomography.

2.2.2 *Triaxial Instrument for Long-Term Deformation and Healing of the Samples*

Experiments were performed under triaxial conditions with $\sigma_1 > \sigma_3 > P_f$ for a timespan of three months. Two identical triaxial instruments were used with the axial stress (σ_A), confining lateral stress (σ_L), fluid pressure (P_f), temperature, and fluid flow rate being independently controlled and monitored over long periods of time, i.e. several months (Fig. 2b), (Hellmann *et al.* 2002a; Le Guen *et al.* 2007). In most cases, the axial stress had the maximum value (corresponding to σ_1) and the confining stress was σ_3. In some cases, however, the lateral stress imposed was slightly higher than the axial stress. Then, the lateral stress was σ_1 and the axial stress σ_3. The

intermediate stress σ_2 was equal to σ_3, because of confinement by a fluid. There are several reasons for using a triaxial state of stress, rather than hydrostatic:

1. under natural conditions, especially near active faults, substantial differential stresses are expected; and
2. strain monitoring is easier under triaxial conditions (by measuring the displacement of the piston) than under hydrostatic conditions.

The axial strain of the samples was measured with high-resolution digital linear encoders (LE/12/SIP50, Solartron) with constant time-steps of 10 min. The sensitivity of the displacement sensors was 0.5 μm. The samples were enclosed in a Viton® sleeve before mounting them in the triaxial cells. The uniaxial stress was imposed by nitrogen gas pressure applied on a piston directly in contact with the sample. The horizontal confining stress was controlled by nitrogen gas pressure applied to the Viton® sleeve. The applied confining stress ranged between 1 and 3 MPa. Given the duration of the experiments (several months), the pressure was not servo-controlled electronically, but pneumatically controlled, using bottles of nitrogen gas at 200 bar pressure. All experiments were performed at 20 °C.

Fluids were injected into the samples by means of a high-pressure liquid chromatography pump (Knauer K-1001 HPLC). The fluid flow rate was constant at 0.3 ml/min during the experiment. The fluid was deionized water with added ammonium chloride (NH_4Cl) at 53.49 g/l, to increase the solubility of the calcite (Ikornikova 1961), and manganese chloride tetrahydrate ($MnCl_2{\cdot}4H_2O$) at 0.90 g/l. The manganese was added to detect any calcite that may have precipitated during the experiment, because when this element is incorporated into newly formed calcite, the calcite has different orange and brown color shades under cathodoluminescence microscopy. First, the injected fluid was prepared in a pressure vessel filled with 25 g calcite grains (diameter 0.315–0.5 mm) in 0.3 l of pure water (Fig. 2b), to saturate the injected solution with calcite.

The solution was subsequently pushed from the pressure vessel into the triaxial cells and circulated from bottom to top of the rock samples. Finally, the solution was collected at the outlet (Fig. 2b). The fluid pressure in the entire system was controlled by use of back-pressure regulators located at the outlet of each triaxial cell (Le Guen *et al*. 2007). The vertical axial strain, confining pressure, and fluid pressure were monitored to determine the deformation of the two samples of Estaillades limestone over a period of 3 months (Table 1). During the first seven weeks, no fluid circulation was imposed, but two injection tests were conducted for 12 h each, imposing an injection rate of 5.10^{-9} m^3 s^{-1}. The fluid pressure at the exit was controlled by use of a back-pressure regulator. During these periods, the values of the axial and confining stresses were maintained more or less constant. This period was used as a reference state to compare the strain values obtained without fluid circulation with those measured in the presence of circulating fluids. During the final 5 weeks, a fluid was injected into the sample at a constant flow rate. Note that some fluid flow bypassed sample C3, because it was severely damaged. For this sample, the confining lateral stress was slowly increased in steps of 0.05–0.1 MPa per day, to better close the vertical fractures. When the fluid pressure was too close to σ_3, some localized circulation occurred at the interface between the sample and the sleeve, dragging some particles there and reducing the fluid pressure. Note also that the fluid was sampled regularly at the outlet and analyzed for its calcium content. These analyses did not reveal any significant variation of calcium content during the course of the experiment.

To compare mechanical behavior and microstructures in the presence of fluid circulation, one dynamically damaged sample (sample C3, 25 mm diameter, 25 mm height) and one sample without damage (sample C1, 25 mm diameter, 50 mm height) were used. The samples were installed in and removed from the two cells at the same time. The fluid flow injection rate was the same for both samples. The experimental conditions (σ_A, σ_L, P_f, T, fluid flow rate, characteristics of the samples) for both samples are summarized in Table 1.

2.2.3 Imaging of Samples in 2D and 3D

Because of progress made in the in-situ observation of rock by use of X-rays and computation,

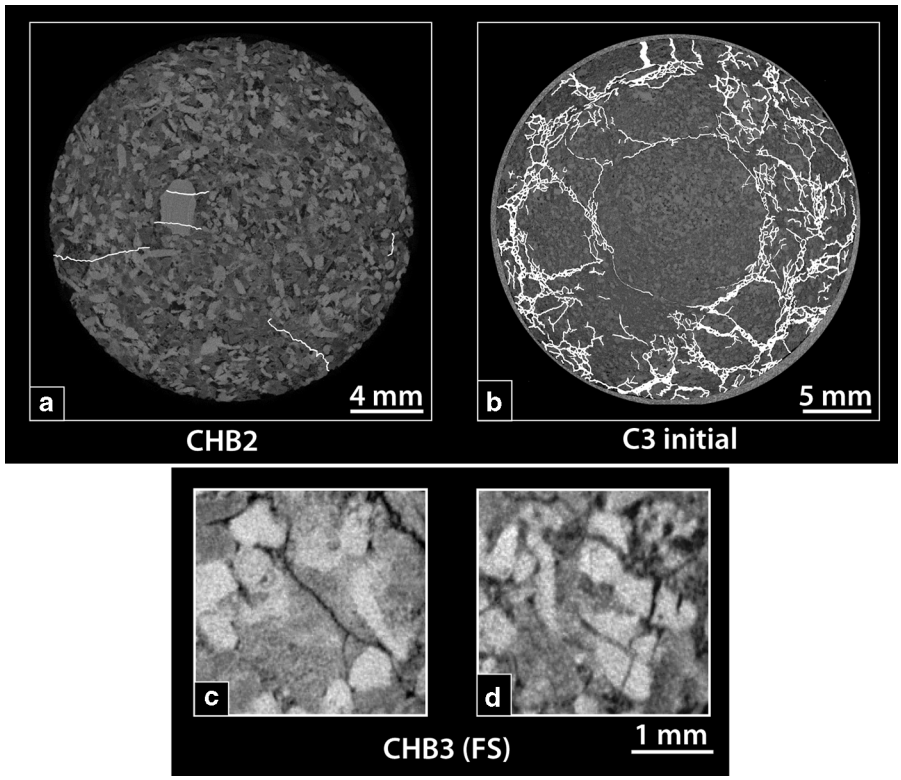

Figure 3
X-ray tomography images of dynamically damaged samples. **a** Sample CHB2 with the lowest fracture density and fracture propagation toward the center of the sample. **b** Sample C3 with the highest fracture density and radial fracture network; the experimental conditions are given in Table 2. The fracture networks are *underlined* with *white lines*. **c**, **d** Magnifications of slices of sample CHB3 showing the two types of fracture propagation: around the grains: intergranular (**c**) and through the grains: intragranular (**d**)

microstructures of samples can be accessed without disadvantages related to the preparation of thin sections, especially destruction of the sample microtomography (Raynaud *et al*. 1989; Géraud *et al.* 1998; Lenoir *et al*. 2007; Renard 2012). A laboratory-built tomograph, installed in the 3S-R laboratory at the University of Grenoble-Alpes, was used to characterize the microstructures of the samples by X-ray microtomography. Voxel resolution was in the range 20–40 μm and the 3D volumes were then analyzed by use of the software AvizoFire.

Tomography acquisition was performed twice for sample C3: after dynamic loading in the SHPB (initial state) and after percolation (final state). Sample C1 was also scanned twice: before (initial state) and after (final state) the percolation experiment. Some complementary data were provided by optical microscopy and field emission gun scanning electron microscopy (FEG-SEM) on thin sections produced from samples after deformation.

Because of the noise level in tomography acquisition, automated segmentation of all fractures could not be performed and tomographic slices had to be processed individually. As a consequence, for each sample, the surface area occupied by the fractures was estimated for four selected X-ray tomography slices and their proportion of the total surface area of the image was calculated. These locations were selected at 20, 40, 60, and 80 % of the total length of the sample. We verified that the fracture density was of the same order of magnitude in these four slices, to estimate the total fracture density of the volume. An average value of the fracture density was also estimated for the initial state of the Estaillades limestone. A damage index is defined as the proportion of fracture surface area in a given tomography

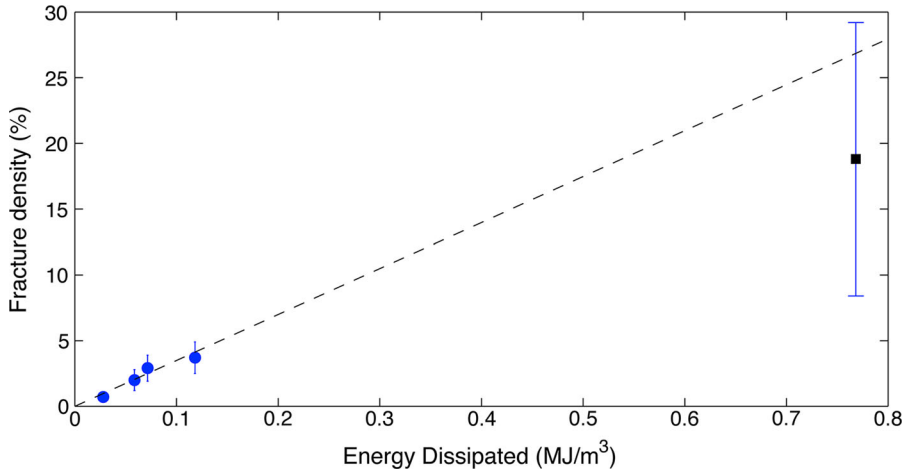

Figure 4
Cross-plot of microstructure fracture density, estimated with X-ray tomography (Table 2), versus dissipated energy, estimated from macroscopic data from the SHPB instrument. The samples tested at ISTerre are marked with *blue circles*, the sample tested at École Polytechnique (C3) is marked with a *black square*. The *dashed line* represents a linear fit, with a slope $\sim$35 %/(MJ/m^3)

slice, at the pixel resolution of the tomography acquisitions; this index is dimensionless and given as a percentage (Table 2).

3. Results

3.1. Dynamic Fracturing: Microstructure Characterization

3.1.1 Effect of Loading on Fracture Density

Fracture densities, measured from tomography data, are related to the loading conditions (Table 2). It was found that the sample impacted with the largest SHPB apparatus, with the highest peak stress and highest strain rate (C3) is the one with the highest fracture density, close to 19 % (Fig. 3b; Table 2). The presence of several crushed areas with a dense network of thin fractures was observed next to areas without any visible fracture. This is indicative of very heterogeneous damage distribution (Fig. 3b). The sample was still cohesive after damaging loading. We therefore believe the sample was close to pulverization. The samples tested with the smallest SHPB device enabled investigation of the formation of damage at lower strain. None of the samples was pulverized, but rather were damaged along few large fractures, either radial or circular. The sample struck with the smallest strain (CHB2) had the smallest fracture density (Fig. 3a; Table 2), close to 0.7 %. Samples CHB1, CHB3 and CHB4 followed this trend with damage indices ranging from 2 to 3.7 %.

We now compare these microstructure descriptions with the macroscopic mechanical data provided by the sensors of the SHPB instrument (Fig. 4). To quantify the energy related to damage mechanism, we computed the surface area below the stress–strain curve, which provides an estimate of the energy dissipated during loading. Despite collection of the two datasets on different scales, they seem to correlate well, both for the samples tested at ISTerre and the sample tested at École Polytechnique.

3.1.2 Effect of Loading on Fracture Geometry

The fracture network has a specific organization. In some places in CHB3 and more generally in CHB2, sparse fractures propagating mainly toward the center of the sample were observed (Fig. 3a). Conversely, main radial fracture zones are found close to the boundary of the sample and form thin circular fracture zones, which do not usually propagate through the center, leaving a relatively undamaged central area (e.g. samples C3, CHB1, CHB4, and part of CHB3; Fig. 3b).

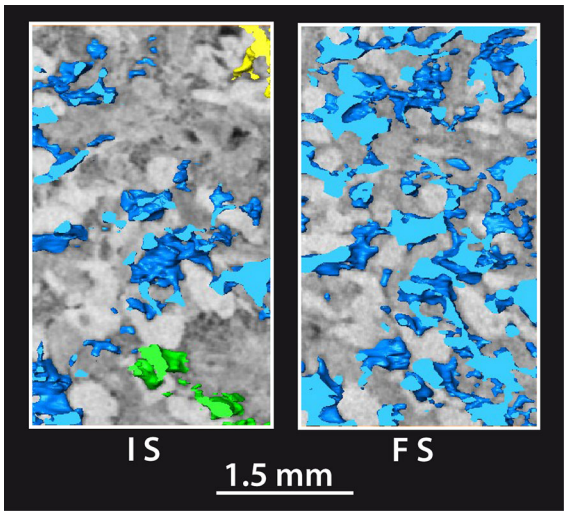

Figure 5
X-ray tomography processed images showing details of the porosity network in 3D for sample CHB3, in its initial state (*IS*) and in its final state after dynamic fracturing (*FS*). The (*colors blue*, *green* and *yellow*) indicate different pores, which are not connected at the grain scale. In the final state, all the pores are connected in a single network, showing that the distance between connected pores has decreased as a result of loading

Two kinds of fracture propagation can be distinguished:

1. intergranular fractures which propagate along grain boundaries and bypass the grains (Fig. 3c); and
2. intragranular fractures cutting through the grains (Fig. 3d).

For the sample with the smallest dissipated energy (CHB2), the fractures propagated easily inside the largest calcitic grains (Fig. 3a), which are the less porous parts of the samples (bright white grains in all the X-ray tomography images). In this case, very few fractures were observed through the smallest grains. Most often, when these small grains are fractured, comparison of the initial and final states revealed they were already fractured before deformation. The samples that were most damaged had additional fractures and were less sensitive to initial heterogeneities. The network of the fractures formed propagated widely through the sample. For these fractures, small grains (most often both calcitic shells and fossil algae) are predominantly broken, rather than larger grains.

3.1.3 *Effect of Loading on Connected Porosity*

On the basis of X-ray tomography images at grain scale, the structure of the pore network was compared before and after dynamic loading (Fig. 5). The porosity could not be quantified in greater detail because of the limited grayscale dynamics of the tomography data. Also pores smaller than the voxel size (20–40 μm) could not be identified. Therefore, only qualitative information is provided here. In the initial state, the pores are not all connected at the grain scale (Fig. 5 IS), but it is known from permeability measurements (Le Guen *et al.* 2007) that they are connected at the scale of the sample as a whole. After loading, most of the pores, which existed before the experiment, are connected at the grain scale and overall porosity is increased (Fig. 5 FS). This indicates that the tortuosity of the flow path between two connected pores has decreased. The newly formed pore networks, connected by the fracture network, are often observed in the dark matrix in the initial state. Because the pore network is directly related to fracture in the damaged samples, the largest pores were identified in samples C3 and CHB4.

3.2. *Fluid Circulation: Enhancement of Dissolution and Healing Processes*

3.2.1 *Total Strain and Creep Rate*

Triaxial instruments were used to study the change in strength and porosity under the effect of both differential stress and reactive-fluid circulation for two samples: one substantially damaged by dynamic fracturing (C3), the other in its initial undeformed state (C1). The axial stress, the confining lateral pressure, and the fluid pressure are plotted in Fig. 6, together with the evolution of the axial strain. The final axial strain ε of the sample was calculated from the axial vertical displacement measured on the X-ray tomography images and defined as $\varepsilon = |l - l_0|/l_0$, where l_0 is the initial sample height and l is the sample height after percolation and deformation. The overall shortening after 3 months was approximately 6 % for sample C1, whereas the overall extensional strain for sample C3 was close to 3 % (Fig. 6). The

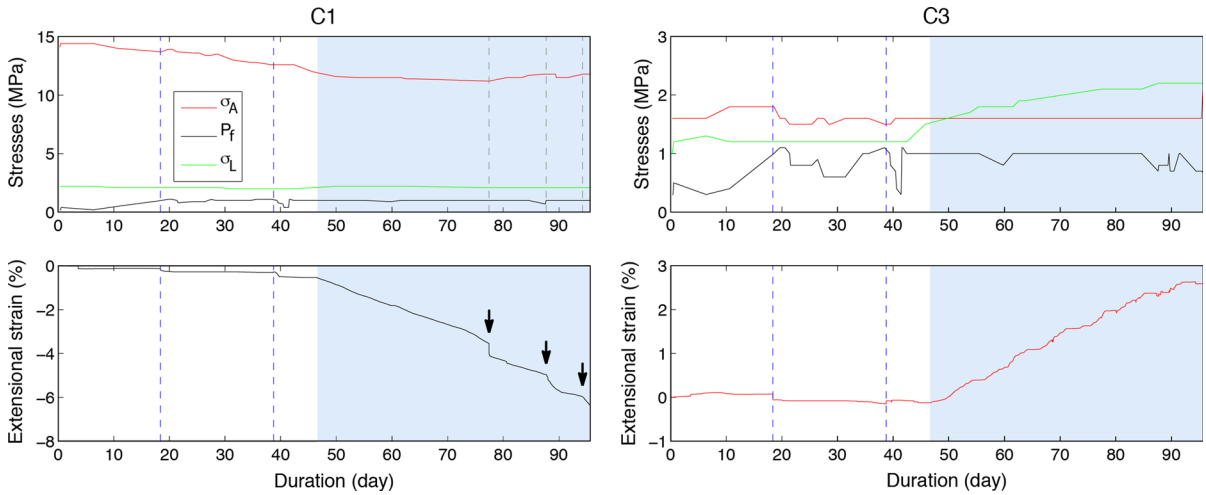

Figure 6
Percolation under stress experiments on non-fractured (C1) and previously fractured (C3) samples. Stresses and cumulative extensional strain curves are shown for both samples for the entire duration of the experiment. The *blue rectangle* highlights the periods of fluid circulation. The two *blue dotted lines* before that period correspond to the first two very short fluid injections through the entire circuit. The *black arrows* on the extensional strain curve for C1 emphasize sudden high-strain events. The corresponding occurrence times are highlighted by *black dotted lines* on the stress data. σ_A is the axial stress, σ_L is the lateral stress, and P_f is the fluid pressure

displacement sensor gave the same result. Moreover, from the displacement data and on the basis of the study by Le Guen *et al*. (2007) using the same triaxial cells and limestone sample, the vertical axial creep rate $\dot{\varepsilon} = (l - l_0)/l_0\Delta t$ was calculated over the entire percolation period (5 weeks). The results are given in Table 1.

The creep rates are similar for both samples (10^{-8} s^{-1} for C1 and 7.1 $\times$ 10^{-9} s^{-1} for C3), although the stress conditions were very different—the ratio of the stress applied to intact sample C1 ($\sim$12 MPa) to that applied to the pre-damaged sample C3 (2 MPa) was 6. Reaching these strain rates may not be reproducible, but the response of the samples to fluid injection and to strain rate is certain.

Both experiments started under dry conditions. For sample C1, the first two short fluid injections caused a rapid response in the strain rate (Fig. 6; the two injections are indicated with dotted black lines). The same response was recorded for the long-duration fluid injection also (Fig. 6, blue area). Axial compaction was observed with some rapid creep events in the cumulative strain curve of sample C1 (arrows in Fig. 6) during the percolation period (starting with the dotted blue line). These high strain rate events occurred for periods ranging from several hours to several days, leading to an increase in the strain rate of several orders of magnitude. Moreover, after these rapid creep events (strain rate in the range 5–9 $\times$ 10^{-8} s^{-1}, compared with the average strain rate of 1.3 $\times$ 10^{-8} s^{-1} over 50 days), the strain curve recovered back to the same slope. These sudden transient creep events in the behavior of C1 observed during the last weeks of percolation cannot be correlated with any systematic variation in fluid pressure. The first event was followed by a slow increase in axial stress, the second event was preceded by a drift in injection fluid pressure, and instantaneously readjusted to the permanent baseline value after the event, and the third event was followed by a change in trend of axial stress. Note that the same value of axial stress resulted in other changes in trend that did not correlate with any significant variation in the other control conditions (i.e. σ_A, σ_L) as shown on the stress curves (Fig. 6).

Concerning the overall strain of sample C3, the method used was the same as that for C1. However, because of the weakness of the damaged sample, a very small difference between the axial stress and the confining lateral stress was imposed at the beginning of the healing experiment. The confining stress was then left to increase toward a value slightly greater

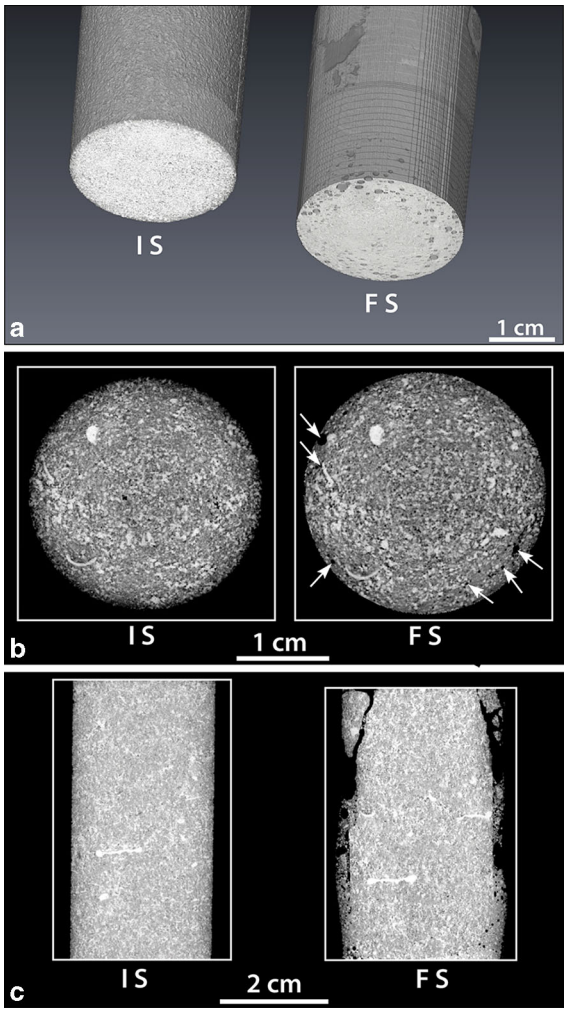

Figure 7
X-ray tomography images of sample C1 (undeformed before healing) **a** 3D images of the initial state (IS) and the final state (FS), showing the pores (*black areas*) that formed at the bottom of the sample. **b** Slice of the same sample as in (**a**), the *white arrows* indicate the pores formed in the final state (FS). **c** 2D cross-sections showing a general comparison between the initial state and the final state, with large pores located at the bottom and small particles deposited between the sample and the sleeve

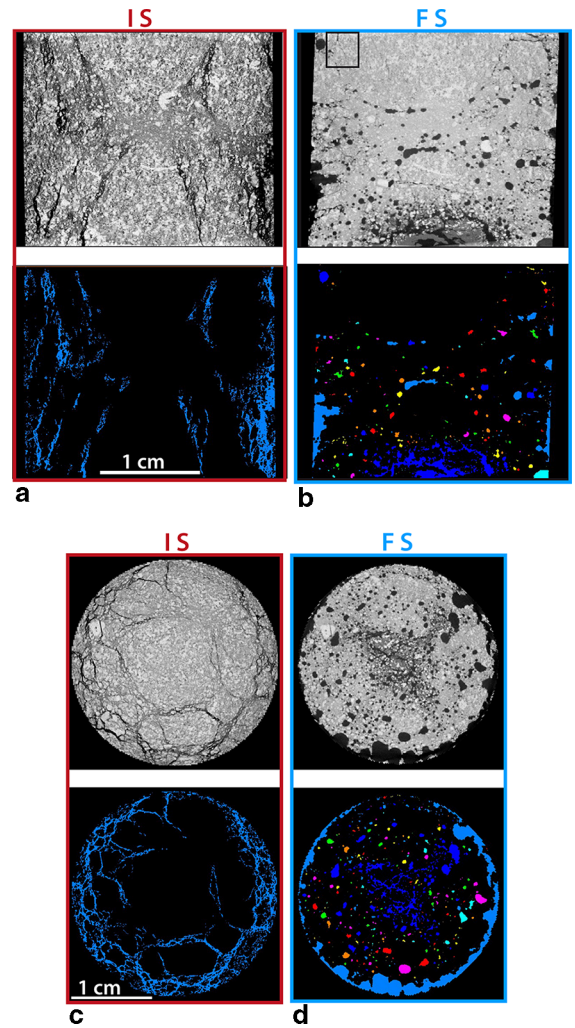

Figure 8
X-ray tomography raw (*top*) and processed (*bottom*) images showing the pattern of open fractures and newly formed porosity (in black on raw images) inside sample C3 damaged (**a**–**c**) before healing (**b**–**d**). The *different colors* on the processed images correspond to pores that are not connected. **a** Damage fracture networks during the initial (fractured) state (IS) in cross-section. **b** Pore networks and healing of the fractures during the final state (FS) in cross-section. The *black square* is the area where the FEG-SEM images of Fig. 12 a–f were taken. **c** Same as (**a**) but in 2D slice view. **d** Same as (**b**) but in 2D slice view

than the axial stress (Fig. 6), to achieve maximum sealing of the vertical fracture network induced during the dynamic stress loading process (Fig. 8, IS). Consequently, the responses to fluid injection occur in the opposite sense for the first short fluid injection and for the long-duration fluid injection because of the shift of the maximum stress from the axial to the lateral direction (Fig. 6). Actually, sample C3 did not shorten but was slightly axially stretched during the long-duration flow-through process with lateral compaction. Through the percolation period, the strain curve of C3 keeps a general constant slope but also contains some slight variations with time that are not correlated with any change in pressure (Fig. 6).

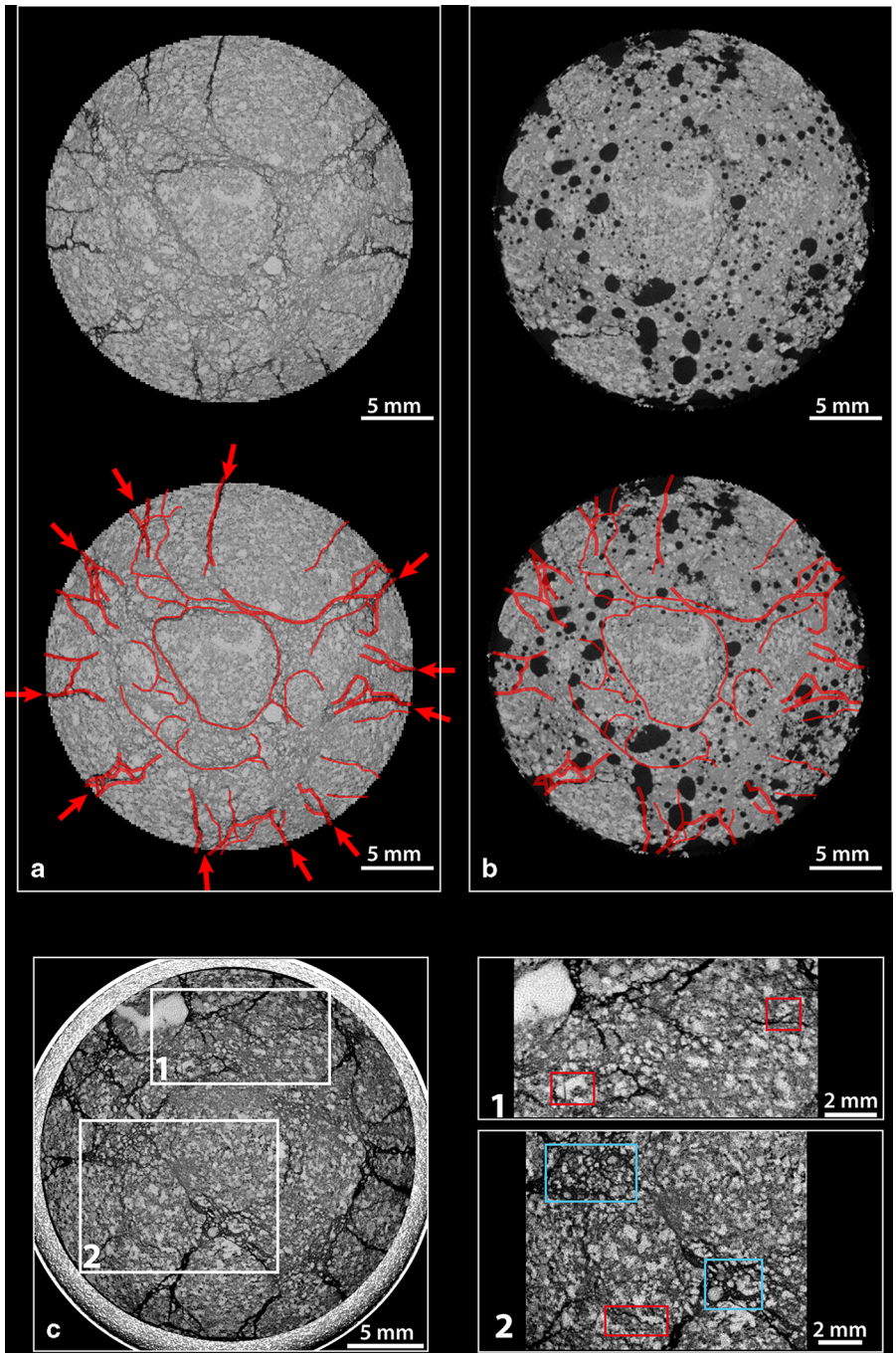

Figure 9
X-ray tomography images of fractured (**a**) and healed (**b**) sample C3. **a** *Top* slice of the initial (fractured) state showing the fracturing network in black. *Bottom* the *red lines* with the *red arrows* indicate the position of the initial main fractures network. **b** *Top* slice of the final state, at the same location. *Bottom* the *red lines* indicate the position of the initial main fractures that subsequently healed. **c** Slice of C3 showing the location of magnifications *1* and *2*. In images *1* and *2* the *red squares* indicate zones of fractures which bypass or break the grains; the *blue squares* indicate zones of crushed areas

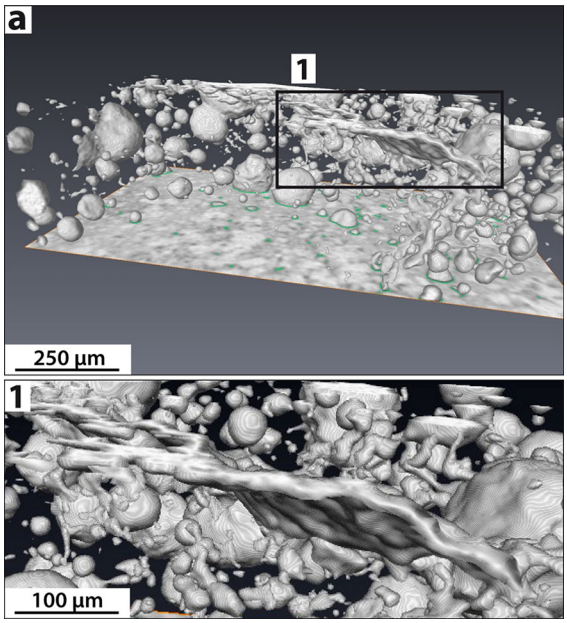

Figure 10
X-ray tomography of processed image showing a 3D sub-volume at the grain scale in sample C3. The newly formed porosity (bubble) and a fracture are displayed in *1*. The porosity network made by the dissolution holes is connected in 3D through thin fractures

3.2.2 *Microstructures in the Undamaged Sample (C1) After Healing*

The X-ray tomography images of sample C1 in its initial and final states after fluid circulation are presented in Fig. 7. At the base of the sample, close to the fluid inlet, some porosity cavities developed over a distance of 5 mm. These large pores have a broad range of sizes, from less than 0.2 to 2.5 mm, and are (on the tomography scale) poorly connected to each other. These pores most probably formed as a result of dissolution of the material (i.e. karstification process), which indicates that the initial fluid was slightly undersaturated with calcite. It should be noted that these pores are located at the bottom of the sample only, i.e. are not observed anywhere else. Similar features have already been observed in the same type of experiment on chalk by Hellmann *et al.* (2002b).

A thin layer of calcite particles forming between the sample and the sleeve near the top of the sample was also observed (Fig. 7). This might be related to predominant fluid circulation between the sample and the sleeve: after percolation through the sample, the finest particles removed from the enlarged pores were carried with the flow. Consequently, when the fluid escaped, these particles became trapped between the sample and the sleeve. Optical microscopy and cathodoluminescence observations on thin sections made from sample C1 confirmed that this unconsolidated aggregate was not a calcite precipitate, but a very thin particle deposit. Indeed, under cathodoluminescence, no difference could be detected between the red shade of the calcite grains of the sample and of those deposited outside the sample.

3.2.3 *Microstructures in the Damaged Sample (C3) After Healing*

For sample C3, the main observation is that the large fractures induced by the dynamic loading process (Fig. 8 IS) were significantly healed after 3 months (Fig. 8 FS). The dense network of different size fractures characterizing the bottom and top of the damaged sample can no longer be seen on the tomographic images taken after the healing process (Figs. 8, 9).

The same dissolution pores as for C1 are observed, but in greater abundance. Some of these large pores follow the traces of the initial fractures (Fig. 8b). Once again, the concentration of these large pores is higher at the base of the sample, where the fluid was injected. In this case however, the large pores spread all the way to the middle of the sample (Fig. 8). These pores appear isolated from each other on this scale.

By comparing the X-ray tomography images of the damaged and healed states, some correlation was found between the main damage fractures and the largest pores (Fig. 9). Nevertheless, as already mentioned above, many of those dissolution pores are not clearly connected to each other and they are not all connected with the fractures (Fig. 10). These connections might be too thin to be detected on the X-ray tomography images at this resolution. However, they are observed at a microscopic scale in thin sections. In the thin sections of C3, the same crushed areas as those shown in Fig. 9 were found and these are directly linked to the largest fractures.

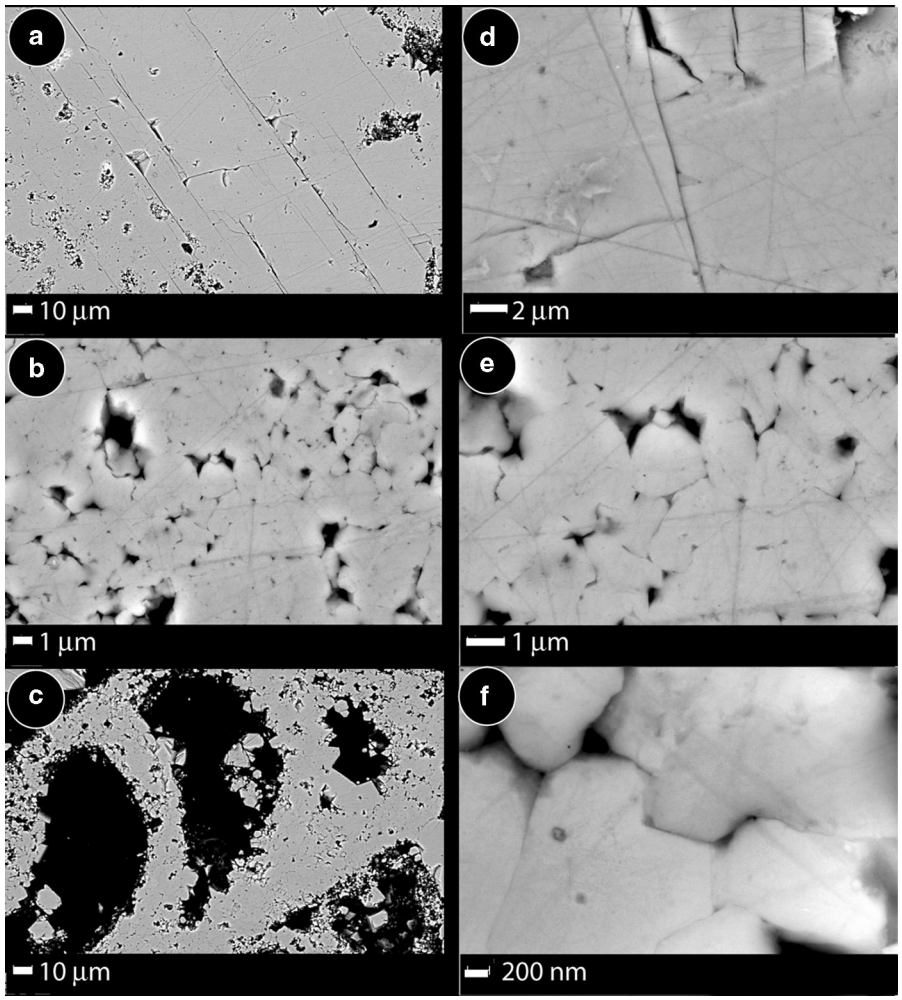

Figure 11
Field-emission gun scanning electron microscope (FEG-SEM) images of Estaillades limestone showing the effect of dynamic loading and healing recovery. **a–f** Initial grain microstructure of sample C1 (flow-through process under static stress on undamaged sample) with a variety of pore densities and sizes and with diagenetic pressure solution indenting: **a**, **d** large grain with fracture porosity, **b**, **e** micrograins with intergranular porosity, **c** fossils with internal structure porosity, **f** grain indenting

3.2.4 SEM Microstructure Comparison of C1 and C3

FEG-SEM observations obtained from thin sections of C1 and C3 were analyzed to investigate both the effect of dynamic loading and the healing recovery process at the microstructure scale. From the observations on the undamaged and healed sample C1, after fluid circulation, three main initial preserved grain microstructures can be distinguished:

1. large grains with intragranular fracture porosity, mostly healed during natural diagenetic processes (Fig. 11a, d);
2. micrograins with grain boundaries, with intergranular porosity and large grain indentations (Fig. 11b, e, f); and
3. large fossil fragments with internal porosity related to the fossil structure (Fig. 11c).

There is no clear evidence of a healing process related to the experimental fluid circulation in this undamaged sample.

To isolate the effect of the dynamic loading on the final microstructures, damaged sample C3 was investigated to see whether it contained the same two main types of structure. The FEG-SEM observations revealed:

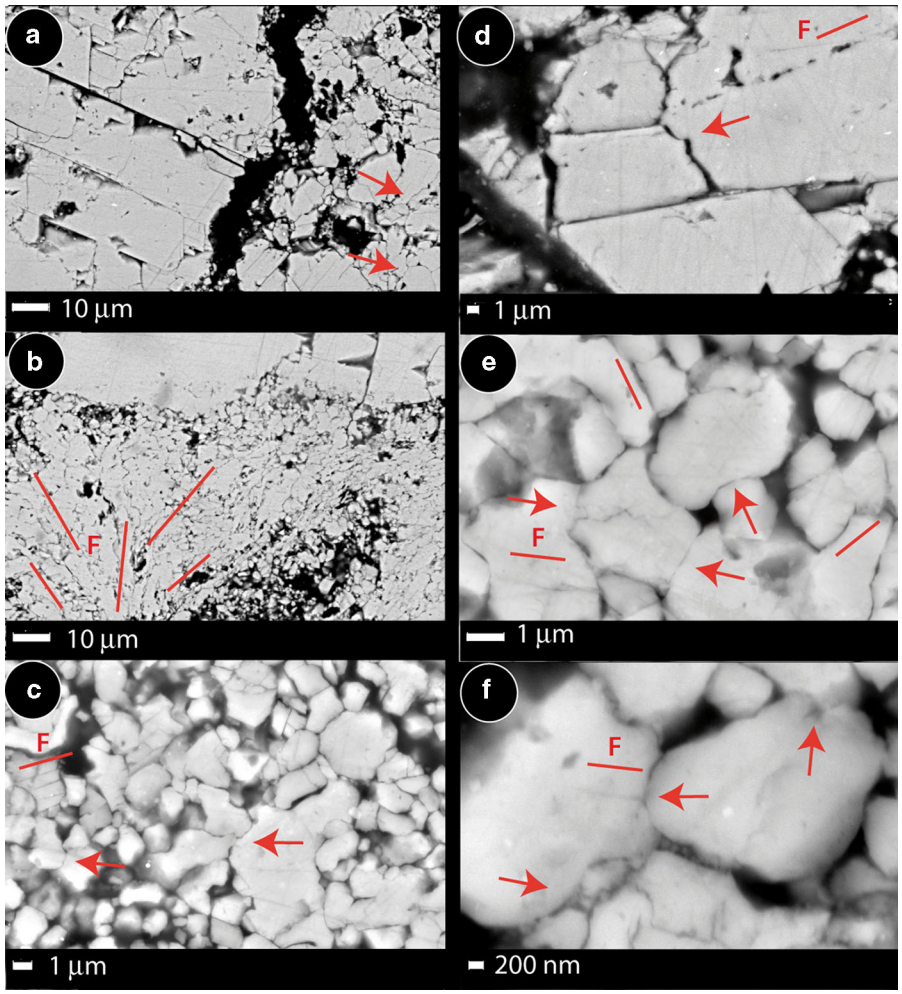

Figure 12
Field-emission gun scanning electron microscope (FEG-SEM) images of Estaillades limestone showing the effect of dynamic loading and healing recovery. **a**, **f** Fractured large grain and dissolution features (*red arrows*) of sample C3, **b**, **e** fan-like fracture network and dissolution indenting between loose grains (*red arrows*), **c**, **f** grain boundary decohesion, and dissolution indenting between loose grains (*red arrows*). (The *black square* in Fig. 8b gives the location of the images in Fig. 12a–f)

1. a more fractured state, with some large main fractures and many small cracks (Fig. 12a, d); and
2. some fan-like fracture networks developed parallel to the principal stress direction of dynamic loading, which are also observed inside the micro-grained structures (Fig. 12b).

Most of the experimentally induced fractures with an aperture of just a few micrometers were healed (Fig. 12f). Of the fractures with larger apertures, several remained open when they were horizontal (parallel to the maximum horizontal confining stress) (Fig. 8) and most closed when they were vertical (perpendicular to the maximum horizontal confining stress). The intergranular porosity is more developed and the grain boundaries more pronounced than in their initial state, leading to clear decohesion and loose grains in some areas (Fig. 12c, e, f), that are related to the dynamic damage effect. Dissolution associated with the sealing effect can be seen at the grain scale only by the indenting of loose grains (Fig. 12e, f) and possibly by dissolution features (stylolite) along some fractures (red arrows Fig. 12a, d).

4. Discussion

4.1. Characterization of Dynamic Fracturing

4.1.1 Damage at the Micro and Macro-Scale

X-ray CT scan images document fractures of aperture greater than voxel size ($\sim$20 μm), whose density defines a damage index. On the other hand, the dissipated energy computed from mechanical data is related to the expansion of fractures at all scales within the sample. Figure 4 show that these two independent datasets are well correlated. Even the most damaged sample, with finely crushed zones, falls on this positive trend, if errors in fracture density estimates are taken into account. This suggests scale independence of damage, and that X-ray images provide a relevant estimate of damage pattern.

The area of the fractures seen on the X-ray images can be computed, and, assuming a fracture energy of $\sim$1 J/m^2, the surface energy related to the fractures visible on the X-ray can be estimated. For instance, for CHB1, the surface energy needed for the creation of the fractures visible on the X-ray image, normalized to the sample volume, amounts to 3 kJ/m^3. This is approximately a factor of 20 less than the dissipated energy computed from mechanical data (72 kJ/m^3; Table 2). This suggests that X-ray images at the resolution used for scanning can only depict 5 % of the total surface area of the fracture created. The missing fracture area may lie in fractures of smaller aperture and in small-scale roughness of the main fractures.

The most comminuted sample C3 has a smaller apparent fracture density than expected from the linear trend of Fig. 4. The additional missing percentage of fracture lies within the finely crushed areas that start to develop at the center of the sample. Despite this contribution, the linear trend between mechanical data and X-ray images suggests that the X-ray imaging technique provides a reliable estimate of fracture pattern changes.

4.1.2 Microstructure Markers of High Strain Rate Damage

With the split Hopkinson pressure bars, samples were loaded at strain rates higher than 50 s^{-1}, when new fracture patterns appear. For instance, the fan-like fracture networks observed on the microstructures of the C3 sample (Fig. 12b), the sample loaded at the highest strain rate, are similar to the branching system described by Sagy *et al.* (2001) as geometric features associated with dynamic fractures. Indeed, the fracture networks resulting from dynamic loading are characterized by a complex geometry and rough edges (Figs. 10, 12a–d) (Sagy *et al.* 2001).

Conversely, fractures across the largest grains in sample C1 (Fig. 11a, d), the reference sample that experienced no additional damage, have a simple straight geometry and smoother edges, which could be attributed to slow growth (i.e. subcritical rate) during diagenetic processes and/or during the percolation experiment. These pre-existing fractures could act as seeds for the fractures developed by dynamic loading (Sagy *et al.* 2001).

4.1.3 Stress Concentration and Strain Localization: Role of Heterogeneities

The loading by split Hopkinson pressure bars is too fast to be servo-controlled. Hence, despite the different striker speeds, the strain rate experienced by the samples tested at ISTerre was the same. The loading history is determined by the intrinsic properties of the samples. Samples CHB1, CHB2, and CHB3 have the same strength (Table 2) and similar fracture patterns: fracturing is poorly developed in the sample and mainly concentrated around the largest calcitic shell grains and pores (Fig. 13a). In general, the main fractures tend to initiate close to large heterogeneities (i.e. grains and pores) and then, to follow grain boundaries or small cracks already present in the sample (Figs. 3c, d, 13b, c).

Conversely, for the sample with the highest impact velocity (C3), localization is less efficient, because the large calcitic shell grains are not damaged (Fig. 13e). This type of behavior has already been noted in a previous study (Doan and Gary 2009) and correlates well with the observation of fracture density organization.

4.2. Characterization of the Healing Process

4.2.1 Strain Variation

The contribution of the three rapid transient creep events represents approximately one third (2 %) of

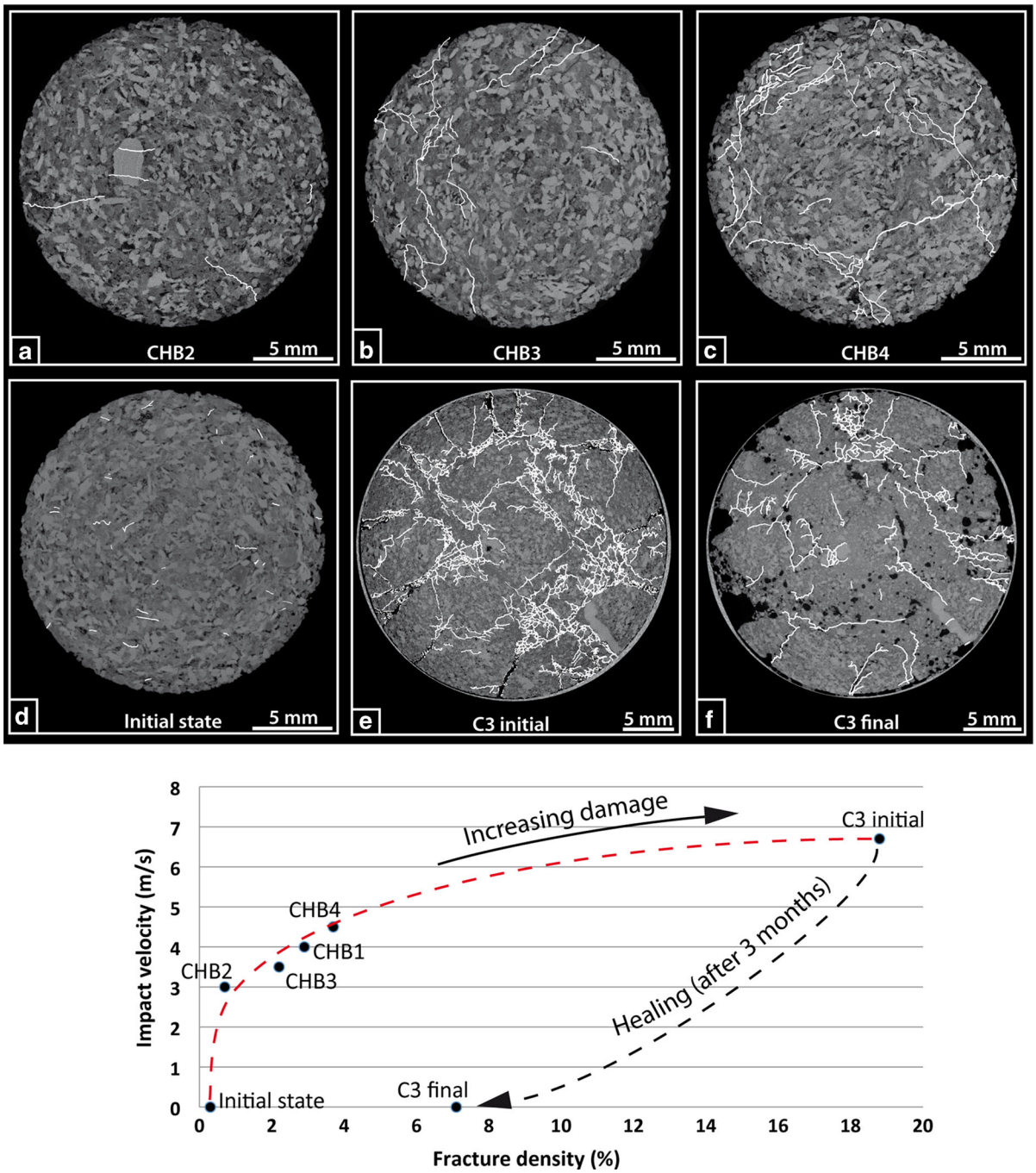

Figure 13

Top: X-ray tomography images: **a–f** illustrate the dependence of fracture density on loading and healing history. The fracture networks are emphasized by *white lines*. *Bottom*: evolution of increasing damage (fracture density %) during dynamic loading of a variety of samples at increasing impact velocity (m/s), and evolution of fracture density with the healing process by percolation under stress (sample C3)

the total strain of sample C1 (6.5 %) (Fig. 6). These sudden creep strain events could be caused by two different effects. On the one hand, high rates of dissolution could cause mechanical collapse of the rock matrix. On the other hand, we cannot rule out the possibility of stick–slip behavior developed by the

Viton piston O-rings on the internal wall of the triaxial cell (Fig. 2b), as previously observed with the same apparatus (Le Guen *et al*. 2007).

The non-regular strain evolution observed for sample C3 shows no correlation with the stresses or with fluid pressure during the percolation period, except around day 90 (Fig. 6). We attribute the cause of this chaotic behavior to the high state of damage of the sample (i.e. the weak cohesion of the grains) and to the low effective axial pressure, such that local grain sliding or damage domain collapse could lead to accelerated deformation for some time periods. Such behavior was not observed for the intact sample C1.

Finally, it is difficult to define the exact effect of the damaged state of sample C3 on the total strain value when comparing it with sample C1 (undamaged), because these two samples have not experienced the same stress history during healing. However, the fractured and crushed state of some areas of C3 could enable stress rotation and pressure solution indenting of the loose grains that can be seen on the FEG-SEM images of Fig. 12e, f. This would lead to grain reorganization at microstructure scale, which easily accommodates the strain on these specific areas.

4.2.2 *Coupling of Dissolution and Healing Processes*

During healing, a large network of pores developed in sample C3 (Fig. 8) compared with the few pores appearing on the 3D reconstruction inside the lower quarter of sample C1 (Fig. 7). For sample C3, these large pores, formed by dissolution, are clearly associated with healing of the main fractures, because the pores are located along the trace of these fractures: the fractures induced by the dynamic loading process (Figs. 8 IS, 9a) were substantially healed after 3 months (Figs. 8 FS, 9). The fracture can no longer be seen on the tomographic images taken after the percolation and deformation process. The pore network is more developed in C3 because fluid circulation was facilitated by the fractures. The average flow rates estimated from the fluid output of the cells are approximately 300 ml/day for C3 and 240 ml/day for C1, thus fluid circulation was faster in the damaged sample (C3). The fractures act as preferred pathways for the fluid, leading to fluid circulation throughout the sample and enhancing the dissolution process, creating a positive feedback loop (Gratier 2011). However, the microstructures and the measured fracture densities of the initial fractured state (18.8 %) and the final healed state (7.1 %) of C3 imply substantial healing during fluid circulation (Fig. 13e, f). The amount of dissolved calcite in the fluid measured from ICP analysis at the inlet of the fluid circuit and at the outlet of both cells is not substantially different and remains constant at approximately 1.5 g/l. Consequently, we propose that dissolution and healing are coupled and lead to the progressive healing of the sample.

Several different healing mechanisms, with or without material supplies, have been observed. They depend on crack aperture, for instance (Gratier *et al*. 2003). The first mechanism, the self-healing of cracks, is a widespread healing process for minerals, driven by reduction of the surface energy of the fractures (Brantley *et al*. 1990; Renard *et al*. 2009b). The fractures progressively heal into a planar layer of fluid inclusions and eventually close completely, leaving a series of unconnected pores. Some very thin pore networks observed in the final state may correspond to fractures in the intermediate state (Fig. 9). The second mechanism, sealing of cracks, closes fractures by deposition of minerals. It has been investigated by thin section observations and cathodoluminescence studies. A luminescence activator (Mn) was used to enhance the luminescence of the calcite deposition, but cathodoluminescence showed no clear evidence of calcite crystallization in the crushed areas of sample C3. Indeed, the intact rocks contained natural fractures filled with calcite with different luminescent colors, which makes it difficult to identify any deposition related to the experiments.

However, observations made with FEG-SEM revealed differences between the microstructure of C1, which are representative of an initial state, and the fractured and healed structures of C3. After characterizing the three main representative initial grain structures of C1 (Fig. 11a–f; discussed in the section "SEM Microstructure Comparison of C1 and C3"), it was possible to distinguish between natural and experimental healing microstructures. Evidence of grain indenting inside the loose grain structures

revealed by FEG-SEM images (Fig. 12e, f) shows that a third healing mechanism can be invoked—solution pressure compaction of the fractured zones. Given the amount of loose-grain areas with grain boundary decohesion associated with the fractured zone (approximately 50 % of the thin section surface area), the healing processes for sample C3 are a combination of mechanical and chemical compaction by pressure solution creep. This healing mechanism is also responsible of the radial compaction of the sample associated with the development of the pore network along the fracture zones. The same combination of different healing processes has already been observed during healing experiments with halite (Bos and Spiers 2002).

Finally, heterogeneities in the rock samples be important in the healing process. The largest pores, located in the same place as the largest fractures, slowed or prevented healing in the vicinity of these heterogeneities. They are the least healed domains. Conversely, the areas protected by the large calcitic shells experienced less strain and were very well healed. The extent of healing is of the same order as the areas corresponding to the crushed material and fine fracturing (Fig. 13e, f). The healing rate thus depends on the fracture and pore dimensions (Brantley *et al.* 1990; Renard *et al.* 2000), but also on grain boundary structures, which affect the dissolution in the pressure solution process and the subsequent healing rate (Hickman and Evans 1991; van Noort *et al.* 2008).

4.3. Applications to Faults

Our experiments confirm that the damage state of a rock strongly affects its mechanical behavior. In the experiments performed here, the fluid circulates faster inside a damaged (fractured) sample than inside an undeformed one, because the main fractures act as preferred flow-channels. The largest fractures accommodate a higher fluid flux, whereas microfracturing enables the fluid to penetrate into the rock mass (Brantley *et al.* 1990; Renard *et al.* 2000). At the scale of a natural fault zone, this effect should increase the kinetics of fluid–rock reactions, as is the case for pressure solution creep (Gratier *et al.* 2011) leading, after some time, to the healing of these fractures. During the entire percolation period (5 weeks), a healing rate of about 0.3 % per day for the most damaged sample (C3) is estimated from the decrease in fracture density between the initial (damaged) state and the final (healed) state. However, the healing rate is rather heterogeneous depending on fracture length and aperture mechanisms.

Application of our results to natural deformation in fault zones must take into account, first, the fact that the solubility of calcite in solution with use of NH_4Cl solution is rather high compared with that in nature and, second, the fact that the width of the fracture, an important property determining rates of healing and sealing, could be smaller in experiments than in nature. Combining these two effects one must contemplate a difference of time scale of at least two orders of magnitude (one order of magnitude because of the different solubility, one order of magnitude because of smaller distance between fractures in experiments). Characteristic healing times in laboratory experiments range from days (for the self-healing process) to more than 100 days for pressure solution compaction and fracture sealing (which was not achieved after this time) leading to natural deformation characteristic healing times ranging from several months to several tens of years, which are plausible. This must be true for limestones. Extension to other rocks containing quartz or feldspar, also likely to be subjected to the same pressure solution compaction and sealing processes, must take into account evolution with temperature (Rutter 1976; Gratier *et al.* 2011).

This difference in characteristic time of healing should lead to the development of large heterogeneities inside the rock mass. Moreover, the rapid healing of the thin crack networks reduces the pore connections and tends to localize the stresses. At the fault scale, the areas strengthened by healing processes could be the places where new brittle deformation is initiated. Thus, healing processes in active faults may determine earthquake recurrence time and the initiation and location of dynamic fracturing (Bos and Spiers 2002).

5. Conclusion

Dynamic damage experiments were performed on five samples of porous Estaillades limestone to

quantify the effect of heterogeneities on the geometry of fracture propagation. Long-term fluid-assisted healing experiments were also performed on two samples of the same limestone, one damaged, the other undamaged, to assess the effect of the damaged state on fluid flow and healing rate. The following conclusions can be drawn from the results obtained.

1. High strain rate loading of samples induced a dense network of fractures. The sample loaded at the highest strain rate was almost pulverized.
2. A relationship is proposed between the fracture density determined from X-ray imaging and the dissipated energy computed from the macro-mechanical data, although these two variables are characterized on different size scales. We propose use of data from X-ray imaging of fracture density as a proxy to quantify damage within the samples.
3. Fracture porosity networks increase and develop on two scales: small fractures enhance the formation of new pathways within the initial porosity network and large fractures increase porosity, creating flow-channels for faster fluid circulation.
4. We believe chemical processes are responsible for closing the fractures, but emphasize that individual mechanisms cannot be separated in the experiments. SEM images show pressure solution creep; tomography data show fracture closing (activated by the presence of fluids); and chemical analysis shows a conservative system: the concentration of calcite at the inlet is the same as at the outlet. All these observations are indicative of chemical effects which result in the observed damage healing.
5. Fluid percolation along a fault zone may lead to the development of a pore network along the fractures that are progressively healed. Candidate mechanisms involve a combination of mechanical and chemical processes (grain sliding, fracture closing, pressure solution creep, crack healing, fracture sealing) that are activated by the presence of reactive fluids.
6. In natural fault zones, the damaged state of rocks has a large effect on the permeability and, consequently, on the kinetics of fluid–rock reactions. The observed heterogeneous healing leads to heterogeneous strengthening of the rocks. As a result, these domains could act as stress concentrators, which should determine the extent of rupture initiation and propagation.

Acknowledgments

We would like to thank Pascal Charrier and Jacques Desrues, Laboratoire 3S-R, UMR 5521 CNRS, Univ. Grenoble-Alpes for the tomography data and Benjamin Vial for technical support. This study was funded by the University Joseph Fourier (AGIR grant) and the Labex OSUG@2020 (Investissement d'Avenir ANR10-LABX56).

References

Ben-Zion, Y., K. Dahmen, V. Lyakhovsky, D. Ertas and A. Agnon, 1999. *Self-Driven Mode Switching of Earthquake Activity on a Fault System*, Earth Planet. Sci. Lett., *172*, 11–21.

Ben-Zion, Y., 2008. *Collective Behavior of Earthquakes and Faults: Continuum-Discrete Transitions, Evolutionary Changes and Corresponding Dynamic Regimes*, Rev. Geophysics, *46*, RG4006, doi:10.1029/2008RG000260.

Bos, B., and Spiers, C.J., 2002. *Fluid-assisted healing processes in gouge-bearing faults: insights from experiments on a rock analogue system*. Pure and Applied Geophysics, *159*: 2537–2566.

Brantley, S.L., Evans, B., Hickman, S.H., and Crerar, D.A., 1990. *Healing of microcracks in quartz: Implications for fluid flow*. Geology, *18*: 136–139.

Chen, W., and Song, B., 2010. Split Hopkinson (Kolsky) Bar: Design, Testing and Application. Springer, Berlin.

Cox, S. F., and Paterson, M.S., 1991. *Experimental dissolution-precipitation creep in quartz aggregates at high temperatures*. Geophysical Research Letters, *18*: 1401–1404.

Dautriat, J., Gland, N., Dimanov, A., and Raphanel, J., 2011, *Hydromechanical behavior of heterogeneous carbonate rock under proportional triaxial loadings*. Journal of Geophysical Research, *116* (B01205), doi:10.1029/2009JB000830.

De Paola, N., Collettini, C., Faulkner, D.R., Trippetta, F., 2008. *Fault zone architecture and deformation processes within evaporitic rocks in the upper crust*. Tectonics, *27*, TC4017, doi:10.1029/2007TC002230.

Dieterich, J.H., and Kilgore, B.D., 1996. *Imaging surface contacts: power law contact distributions and contact stresses in quarts, calcite, glass, and acrylic plastic*. Tectonophysics, *256*, 219–239.

Doan, M.-L., and Billi, A., 2011. *High strain rate damage of Carrara marble*. Geophysical Research Letters, *38*, L19302, doi:10.1029/2011GL049169.

Doan, M.-L., and Gary, G., 2009. *Rock pulverization at high strain rate near the San Andreas fault*. Nature Geoscience, *2*: 709–712, doi:10.1038/NGEO640.

Dor, O., Chester, J.S., Ben-Zion, Y., Brune, J.N., and Rockwell, T.K., 2009. *Characterization of damage in sandstones along the Mojave section of the San Andreas Fault: Implications for the shallow extent of damage generation*. Pure and Applied Geophysics, *166*: 1747–1773, doi:10.1007/s00024-009-0516-z.

Dor, O., Ben-Zion, Y., Rockwell, T.K., and Brune, J., 2006a. *Pulverized rocks in the Mojave section of the San Andreas Fault Zone*. Earth and Planetary Science Letters, *245*: 642–654.

Dor, O., Rockwell, T.K., and Ben-Zion, Y., 2006b. *Geologic observations of damage asymmetry in the structure of the San Jacinto, San Andreas and Punchbowl faults in southern California: a possible indicator for preferred rupture propagation direction*. Pure and Applied Geophysics, *163*: 301–349, doi:10.1007/s00024-005-0023-9.

Faulkner, D.R., Jackson, C.A.L., Lunn., R.J., Schlische, R.W., Shipton, Z.K., Wibberley, C.A.J., and Withjack, M.O., 2010. *A review of recent developments concerning the structure, mechanics and fluid flow properties of fault zones*. Journal of Structural Geology, *32*: 1557–1575.

Faulkner, D.R., Mitchell, T.M., Healy, D., and Heap, M.J., 2006. *Slip on 'weak' faults by the rotation of regional stress in the fracture damage zone*. Nature, *444*: 922–925, doi:10.1038/nature05353.

Faulkner, D.R., Lewis, A.C., and Rutter, E.H., 2003. *On the internal structure and mechanics of large strike-slip fault zones: field observations of the Carboneras fault in southeastern Spain*. Tectonophysics, *367*: 235–251.

Géraud, Y., Mazerolle, F., Raynaud, S., and Lebon, P., 1998. *Crack location in granitic samples submitted to heating, low confining pressure and axial loading*. Geophysical Journal International, *133*: 553–567.

Gratier, J.-P., 2011. *Fault permeability and strength evolution related to fracturing and healing episodic processes (years to millennia): the role of pressure solution*. Oil & Gas Science and Technology–Rev. IFP Energies Nouvelles, *66*: 491–506.

Gratier, J.-P., Richard, J., Renard, F., Mittempergher, S., Doan, M.-L., Di Toro, G., Hadizadeh, J., and Boullier, A.-M., 2011. *Aseismic sliding of active faults by pressure solution creep: Evidence from the San Andreas Fault Observatory at Depth*. Geology, *39*: 1131–1134.

Gratier, J.-P., Favreau, P., and Renard, F., 2003. *Modeling fluid transfer along California faults when integrating pressure solution crack sealing and compaction processes*. Journal of Geophysical Research, *108*, B2, 2104, doi:10.1029/2001JB000380.

Gratier, J.-P., Renard, F., and Labaume, P., 1999. *How pressure solution creep and fracturing processes interact in the upper crust to make it behave in both a brittle and viscous manner*. Journal of Structural Geology, *21*: 1189–1197.

Gratier, J.-P., Renard, F., and Vial, B., 2014. *Postseismic pressure solution creep: evidence and time-dependent change from dynamic indenting experiments*, Journal of Geophysical Research, doi:10.1002/2013JB010768.

Han, M., Fleury, M., and Levitz, P., 2007. Effect of the pore structure on resistivity index curves. International Symposium of the Society of Core Analysts, Calgary, Canada.

Hickman, S.H., and Evans, B., 1991. *Experimental pressure solution in halite: the effect of grain/interphase boundary structure*. Journal of the Geophysical Society, London, *148*: 549–560.

Hellmann, R., Renders, P.J.N., Gratier, J.-P., and Guiguet, R., 2002a. *Experimental pressure solution compaction of chalk in aqueous solutions. Part 1. Deformation behavior and chemistry*. The Geochemical Society, Special Publication, *7*: 129–152.

Hellmann, R., Gaviglio, P., Renders, P.J.N., Gratier, J.-P., Békri, S., and Adler, P., 2002b. *Experimental pressure solution compaction of chalk in aqueous solutions. Part 2. Deformation examined by SEM, porosimetry, synthetic permeability, and X-ray computerized tomography*. The Geochemical Society, Special Publication, *7*: 153–178.

Ikornikova, N.Y., 1961. *The process of solution of calcite in aqueous solution of chlorides at high temperatures and pressures*. Soviet Phys. Crystallogr., *5*: 726–733.

Karner, S.L., Marone, C., and Evans, B., 1997. *Laboratory study of fault healing and lithification in simulated fault gouge under hydrothermal conditions*. Tectonophysics, *227*: 41–55.

Lenoir, N., Bornert, M., Desrues, J., Bésuelle, P., and Viggiani, G., 2007. *Volumetric digital image correlation applied to X-ray microtomography images from triaxial compression tests on argillaceous rock*. Strain, *43*: 193–205, doi:10.1111/j.1475-1305.2007.00348.x.

Lyakhovsky, V., Y. Ben-Zion and A. Agnon, 2001. *Earthquake Cycle, Fault Zones, and Seismicity Patterns in a Rheologically Layered Lithosphere*, J. Geophys. Res., *106*, 4103–4120.

Le Guen, Y., Hellmann, R., Collombet, M., Gratier, J.-P., Renard, F., and Brosse, E., 2007. *Enhanced deformation of limestone and sandstone in the presence of high PCO2 fluids*. Journal of Geophysical Research B: Solid Earth, *112*, B05421, doi:10.1029/2006JB004637.

Moore, D.E., Lockner, D.A., Byerlee, J.D, 1994, *Reduction of permeability in granite at elevated température*, Science, *265*, 1558–1561.

Morrow, C.A., Moore, D.E., Lockner, D.A., 2001, *Permeability reduction in granite under hydrothermal conditions* Journal of Geophysical Research: Solid Earth, *106*, B12, 30551–30560.

Nakatani, M., and Scholz, C.H., 2004. *Frictional healing of quartz gouge under hydrothermal conditions: 1. Experimental evidence for solution transfer healing mechanism*. Journal of Geophysical Research – Solid Earth, *109*, B07201.

Niemeijer, A., Marone, C., and Elsworth, D., 2008. *Healing of simulated fault gouges aided by pressure solution: results from rock analogue experiments*. Journal of Geophysical Research, *113*, B04204, doi:10.1029/2007JB005376.

van Noort, R., Visser, H.J.M., and Spiers, C.J., 2008. *Influence of grain boundary structure on dissolution controlled pressure solution and retarding effects of grain boundary healing*. Journal of Geophysical Research, *113*, B03201, doi:10.1029/2007JB005223.

Peng, Z. and Y. Ben-Zion, 2006. *Temporal changes of shallow seismic velocity around the Karadere-Duzce branch of the north Anatolian fault and strong ground motion*, Pure Appl. Geophys., *163*, 567–600, doi:10.1007/s00024-005-0034-6.

Raj, R., 1982. *Creep in polycrystalline aggregates by matter transport through a liquid phase*. Journal of Geophysical Research-Solid Earth, *87*: 4731–4739.

Ravi-Chandar, K., and Knauss, W.G., 1984a. *An experimental investigation into dynamic fracture: I. Crack initiation and arrest*. International Journal of Fracture, *25*: 247–262.

Ravi-Chandar, K., and Knauss, W.G., 1984b. *An experimental investigation into dynamic fracture: II. Microstructural aspects*. International Journal of Fracture, *26*: 247–262.

Raynaud, S., Fabre, D., Mazerolle, F., Géraud, Y., and Latière, H.J., 1989. *Analysis of the internal structure of rocks and*

characterization of mechanical deformation by a non-destructive method: X-ray tomodensitometry. Tectonophysics, *159*: 149–159.

Reches, Z., and Dewers, T.A., 2005. *Gouge formation by dynamic pulverization during earthquake rupture*. Earth and Planetary Science Letters, *235*: 361–374.

Renard, F., 2012. *Microfracturation in rocks: from microtomography images to processes*. European Physical Journal Applied Physics, *60*: 24203, doi:10.1051/epjap/2012120093.

Renard, F., Bernard, D., Desrues, J., and Ougier-Simonin, A., 2009a. *3D imaging of fracture propagation using synchrotron X-ray microtomography*. Earth and Planetary Science Letters, *286*: 285–291, doi:10.1016/j.epsl.2009.06.040.

Renard, F., Dysthe, D.K., Feder, J.G., Meakin, P., Morris, S.J.S., and Jamtveit, B., 2009b. *Pattern formation during healing of fluid-filled cracks: an analog experiment*. Geofluids, *9*: 365–372, doi:10.1111/j.1468-8123.2009.00260.x.

Renard, F., Gratier, J.-P., Jamtveit, B., 2000. *Kinetics of crack-sealing, intergranular pressure solution, and compaction around active fault*. Journal of Structural Geology, *22*: 1395–1407.

Rutter, E.H., Maddock, R.H., Hall, S.H., and White, S.H., 1986. *Comparative microstructures of natural and experimentally produced clay-bearing fault gouges*. Pure and Applied Geophysics, *124*: 3–30.

Rutter, E.H., 1976. *The kinetics of rock deformation by pressure solution*. Philosophical Transactions of the Royal Society of London, *283*: 203–219.

Sagy, A., Reches, Z., and Roman I., 2001. *Dynamic fracturing: field and experimental observations*. Journal of Structural Geology, *23*: 1223–1239.

Sleep, N.H., and Blanpied, M.L., 1992. *Creep, compaction and the weak rheology of major faults*. Nature, *359*: 687–692.

Tenthorey, E., and Cox, S., 2006. *Cohesive strengthening of fault zones during the interseismic period: An experimental study*. Journal of Geophysical Research, *111*, B09202, doi:10.1029/2005JB004122.

Tenthorey, E. and Fitzgerald J.D., 2006. *Feedbacks between deformation, hydrothermal reaction and permeability evolution in the crust: Experimental insights*, Earth and Planetary Science Letters, *247*, 1–2, 117–129.

Wechsler, N., Allen, E.E., Rockwell, T.K., Girty, G., Chester, J.S., and Ben-Zion, Y., 2011. *Characterization of pulverized granitoids in a shallow core along the San Andreas Fault, Littlerock, CA*. Geophysical Journal International, *186*: 401–417.

Weyl, P.K., 1959. *Pressure solution and the force of crystallization: a phenomenological theory*. Journal of Geophysical Research, *64*: 2001–2025.

Wu, C. Z. Peng and Y. Ben-Zion, 2009. *Non-linearity and temporal changes of fault zone site response associated with strong ground motion*, Geophys. J. Int., *176*, 265–278, doi:10.1111/j.1365-246X.2008.04005.x.

Yasuhara, H., Marone, C., and Elsworth, D., 2005. *Fault zone restrengthening and frictional healing: the role of pressure solution*. Journal of Geophysical Research, *110*, B06310, doi: 10.1029/2004JB003327.

Yuan, F., Prakash, V., and Tullis, T., 2011. *Origin of pulverized rocks during earthquake fault rupture*. Journal of Geophysical Research, *116*, B06309, doi:10.1029/2010JB007721.

(Received January 28, 2014, revised October 8, 2014, accepted October 9, 2014, onlinedate November 16, 2014)